

MIT Open Access Articles

Application of the SPH method to solitary wave impact on an offshore platform

The MIT Faculty has made this article openly available. **Please share** how this access benefits you. Your story matters.

Citation: Pan, K. et al. "Application of the SPH Method to Solitary Wave Impact on an Offshore Platform." Computational Particle Mechanics 3.2 (2016): 155–166.

As Published: <http://dx.doi.org/10.1007/s40571-015-0069-0>

Publisher: Springer International Publishing

Persistent URL: <http://hdl.handle.net/1721.1/103305>

Version: Author's final manuscript: final author's manuscript post peer review, without publisher's formatting or copy editing

Terms of use: Creative Commons Attribution-Noncommercial-Share Alike



Application of the SPH Method to Solitary Wave Impact on an Off-shore Platform

K. Pan¹ · R. H. A. IJzermans²
B. D. Jones¹ · A. Thyagarajan²
B. W. H. van Beest² · J. R. Williams¹

Received: date / Accepted: date

Abstract This paper investigates the interaction between large waves and floating offshore structures. Here, the fluid-structure interaction is considered using the weakly compressible smoothed particle hydrodynamics (SPH) method. To ensure the applicability of this method, we validate its prediction for fluid forces and rigid-body motion against two sets of experimental data. These are impact due to dam-break, and wave induced motion of a floating cube. For the dam break problem, the SPH method is used to predict impact forces on a rectangular column located downstream. In the second case of a floating cube, the SPH method simulates the motion of a buoyant cube under the action of induced waves, where a wall placed upstream of the cube is displaced sinusoidally to induce waves. In both cases, the SPH framework implemented is able to accurately reproduce the experimental results. Following validation, we apply this framework to simulation of a toy model of a tension leg platform upon impact of a large solitary wave. This analysis shows that the platform may be pulled into the water by stretched tension legs, where the extension of the tension legs also governs the rotational behavior of the platform. The result also indicates that a tension-leg platform is very unlikely to topple over during the arrival of an extreme wave.

Keywords Smoothed Particle Hydrodynamics · Free surface flow · Fluid-Structure interaction · Tension-leg platform

¹Massachusetts Institute of Technology
77 Massachusetts Ave., Cambridge
MA 02139
USA
E-mail: pkpan@mit.edu

²Shell Technology Centre Bangalore,
8b Kundalahalli Main Road, Bangalore 560048,
India.

1 Introduction

In offshore hydrocarbon production, a platform from which drilling and production activities occur will be placed in one location for many years, typically decades. These structures must survive all weather types, including rogue waves, large swells, and heavy storms. In recent work, the European space agency identified more than 10 rogue waves, over 25 m high, in a period of just three weeks [1]. This demonstrates that such waves are a real danger to shipping and other offshore industries. The highly non-linear impact of a rogue wave on a floating, moored offshore structure is a problem that has significant practical application in the safety of offshore oil and gas production.

Accurate knowledge of response to rogue waves is therefore a fundamental component of offshore structure design. Lab tests with scale models are frequently used to determine hydrodynamic forces, but they are both expensive and time consuming. As such, the behavior of offshore structures subject to extreme waves cannot be studied by small-scale model experiments easily. So computational tools for the prediction of local wave impact loads and overall motion of the structure are desirable.

Smoothed Particle Hydrodynamics (SPH) is a mesh-free, fully Lagrangian method for numerical simulation of fluid flow [2–5]. In the SPH method, a computational domain is discretized by a set of points, or *particles*, and a meshless discretization scheme is used to represent a scalar or vector field in terms of its values at these points. Since the particles are advected with the flow field, the SPH is ideally suited to problems of free surface flow, where computationally expensive surface tracking, typically required by continuum approaches, is not necessary [2].

Before applying the SPH method to real world problems, we first demonstrate that the SPH simulation can accurately predict the impact force on fixed structures and rigid-body motion. A three-dimensional dam break case has been simulated and we compare the calculated load on a tall column to those measured during an experiment by Yeh and Petroff [6]. This configuration has proven to be a popular test case for benchmarking free surface flow algorithms, and appears as a validation case to indicate the ability of the SPH method to capture loading characteristics in violent gravity-driven fluid-structure interactions [7, 8]. Following analysis of fixed structure impacts, we consider the motion of a floating body, under the action of induced waves [9, 10]. The SPH method accurately reproduces the experimental data, demonstrating the advantages of the SPH in simulating free-surface-flow and floating structure interaction. Finally, as a proof of concept, we apply our SPH framework to simulate the effect of a solitary wave on a tension-leg platform. We simulate the force acting on the platform under the effect of a sea wave and stretched tension legs. This simulation can serve as a blueprint for more advanced simulations in the future.

2 Methodology

In the SPH technique, the continuum is represented by a set of discrete particles, characterized by their own physical properties such as mass, density, and pressure [2–5]. In SPH, the fundamental principle is to approximate any function $A(\mathbf{r})$ by an integral interpolant

$$A(\mathbf{r}) = \int A(\mathbf{r}')W(\mathbf{r} - \mathbf{r}', h)d\mathbf{r}' \quad (1)$$

where $W(\mathbf{r} - \mathbf{r}', h)$ is the weighting function or *kernel* and h is the so-called *smoothing length*. In discrete notation, this becomes

$$\langle A(\mathbf{r}) \rangle = \sum_b \frac{m_b}{\rho_b} A_b W_{ab} \quad (2)$$

where the summation is over all particles b within the compact support domain of the kernel function W at particle a . m_b and ρ_b , respectively, are the mass and the density of particle b .

A quintic spline kernel function has been used following Morris [11] such that, with $R = |\mathbf{r}_i - \mathbf{r}_j|/h$

$$W_{ab} = \alpha_d \times \begin{cases} (3-R)^3 - 6(2-R)^2 + 15(1-R)^5 & 0 \leq R \leq 1; \\ (3-R)^3 - 6(2-R)^2 & 1 \leq R \leq 2; \\ (3-R)^3 & 2 \leq R \leq 3; \\ 0 & 3 \leq R. \end{cases} \quad (3)$$

where $\alpha_d = 120/h$, $\alpha_d = 7/(478\pi h^2)$, $\alpha_d = 3/(359\pi h^3)$ in 1, 2 and 3 dimensions, respectively.

The particle velocities are determined from the discretization of the Navier-Stokes momentum equation

$$\frac{D\mathbf{v}}{Dt} = -\frac{1}{\rho}\nabla p + \mathbf{g} + \Theta \quad (4)$$

where p is the pressure, \mathbf{g} is the gravity acceleration and Θ is the dissipative term.

In SPH notation, Eq. (4) can be written as

$$\frac{D\mathbf{v}_a}{Dt} = -\sum_b m_b \left(\frac{p_a}{\rho_a^2} + \frac{p_b}{\rho_b^2} + \Pi_{ab} \right) \nabla_a W_{ab} + \mathbf{g} \quad (5)$$

in which p_a and ρ_a denote the pressure and density of particle a . Π_{ab} represents an artificial viscosity model, where we use the model proposed by Monaghan [2] which is defined as

$$\Pi_{ab} = \begin{cases} \frac{\alpha \bar{c}_{ab} h}{\rho_{ab}} \frac{\mathbf{v}_{ab} \cdot \mathbf{r}_{ab}}{\mathbf{r}_{ab}^2 + \epsilon h^2} & \mathbf{v}_{ab} \cdot \mathbf{r}_{ab} < 0; \\ 0 & \mathbf{v}_{ab} \cdot \mathbf{r}_{ab} \geq 0. \end{cases} \quad (6)$$

where $\mathbf{r}_{ab} = \mathbf{r}_a - \mathbf{r}_b$, $\mathbf{v}_{ab} = \mathbf{v}_a - \mathbf{v}_b$, with the position \mathbf{r}_k and velocity \mathbf{v}_k of particle k , $\bar{c}_{ab} = (c_a + c_b)/2$, $\epsilon = 0.01$. The artificial viscosity coefficient, α , has the main purpose of preventing instability and spurious oscillations in the numerical scheme. For phenomena such as wave impact on offshore structures, α has little influence on the main characteristics of the flow [8, 12–14]. The value of $\alpha = 0.1$ was adopted in this work unless stated otherwise. This choice of α gives stable numerical results for all test cases and the result agrees with experimental measurement well. Eq. (5) was used to update the accelerations of fluid particles.

Changes in the fluid density were calculated by means of discretizing the mass continuity equation,

$$\frac{D\rho}{Dt} = -\rho \nabla \cdot \mathbf{v} \quad (7)$$

which, in SPH formulation, reads

$$\frac{D\rho_a}{Dt} = \sum_b m_b (\mathbf{v}_a - \mathbf{v}_b) \cdot \nabla_a W_{ab} \quad (8)$$

where $\nabla_a W_{ab}$ is the gradient of the kernel function. Compared to an alternative way to compute the density field based on weighted summation of mass terms [15], the method described in Eq. (8) is more suitable for free surface flow simulation as it prevents artificial density decrease near boundaries and near free surfaces [2, 13].

The acceleration depends on the pressure, which, for a weakly compressible fluid, is usually specified by an equation of state [16] of the form

$$p = \frac{c_0^2 \rho_0}{\gamma} \left[\left(\frac{\rho}{\rho_0} \right)^\gamma - 1 \right] \quad (9)$$

where ρ_0 is the reference density of the fluid and c_0 is the speed of sound at the reference density, p is the pressure. In the calculations to be described here, $\gamma = 7$ [2]. In the numerical scheme the speed of sound c_0 is set equal to at least 10 times the maximum velocity expected in order to obtain reasonable time steps and also keep the density variation within 1% compared to the reference density [3].

Discretisation in time is carried out with the Verlet time integration scheme [13]. The time-step Δt is calculated according to the Courant-Friedrichs-Lewy (CFL) condition, the force term and the viscous diffusion term. A variable time step Δt was calculated according to [13]

$$\Delta t = CFL \cdot \min(\Delta t_f, \Delta t_{cv}) \quad (10)$$

with

$$\Delta t_f = \min_a (\sqrt{h/|f_a|}) \quad \Delta t_{cv} = \min_a \frac{h}{c_s + \max_b \left| \frac{h \mathbf{v}_{ab} \cdot \mathbf{r}_{ab}}{|\mathbf{r}_{ab}|^2 + \epsilon h^2} \right|} \quad (11)$$

where $|f_a|$ is the force magnitude per unit mass of particle a . Δt_{cv} combines the CFL condition and the viscous time-step controls. In this work $CFL = 0.3$ is used.

In the SPH literature, various methods exist for the discretization of solid boundary conditions [17]. The *dynamic boundary particles* method is adopted in this work, where boundary particles (BPs) satisfy the same equations of continuity and state as the fluid particles (FPs), but their position remains unchanged (fixed boundaries) or is externally imposed (moving objects like wavemakers). When a FP approaches a boundary and the distance between the BP and the FP becomes smaller than the kernel function range, the density of the BP increases resulting in pressure increase. Thus, the force exerted on the FP increases due to the pressure term in the momentum equation. This method allows to easily discretize complex domains and leads to an acceptable compromise between accuracy and computational costs. For a complete description of the mechanism the reader is referred to [18].

In this paper we use equations describing rigid body dynamics in general 3D case by adopting the *rotation matrix* approach. Since this theory is explained in many textbooks on Newtonian dynamics [19], we just directly present the major equations here. In the mathematical description of rigid body motion, it is convenient to work with two different reference frames: a *world* frame, which remains fixed in time and an *object* frame, which moves and rotates with the rigid body. We denote coordinates in the world frame by $\mathbf{x} = (x, y, z)$, whereas the coordinates in the object frame are denoted by $\boldsymbol{\xi} = (\xi, \eta, \zeta)$. The origin of the object frame is kept equal to the centre-of-mass (COM) of the floating object. Any coordinate in the object frame, $\boldsymbol{\xi}$, can be translated into world frame coordinates \mathbf{x} as follows

$$\mathbf{x} = \mathbf{x}_{com} + \mathbf{R}\boldsymbol{\xi}, \quad (12)$$

where \mathbf{x}_{com} is the displacement of COM of a rigid body and \mathbf{R} is the so-called rotation matrix. The rotation matrix is composed of the projections of the unit vectors \mathbf{e}_ξ , \mathbf{e}_η , \mathbf{e}_ζ onto the world coordinate axes \mathbf{e}_x , \mathbf{e}_y , and \mathbf{e}_z . The motion of \mathbf{x}_{com} is given by

$$\frac{d\mathbf{x}_{com}}{dt} = \mathbf{v}_{com}, \quad \frac{d\mathbf{v}_{com}}{dt} = \mathbf{F}/m \quad (13)$$

where \mathbf{v}_{com} is the velocity of COM, \mathbf{F} is the total force acting on the floating object and m is the mass of the floating object. The total force \mathbf{F} on a floating object can be computed by summing the contributions exerted on the boundary particles for an entire body. Assuming that the objects are treated as rigid bodies, the force on each BP is computed by summing up the contribution from all the surrounding FPs within the surrounding kernel. Hence, BP k experiences a force per unit mass given by

$$\mathbf{f}_k = \sum_{a \in FPs} \mathbf{f}_{ka} \quad (14)$$

where \mathbf{f}_{ka} is the force per unit mass exerted by FP a on BP k . By the principle of equal and opposite action and reaction, the force exerted by a FP on each BP is given by

$$m_k \mathbf{f}_{ka} = -m_a \mathbf{f}_{ak} \quad (15)$$

where \mathbf{f}_{ak} is just the contribution component of BP k to the term $\frac{D\mathbf{v}_a}{Dt}$ in Eq. (5). The total force \mathbf{F} on a floating object is then computed as

$$\mathbf{F} = \sum_{k \in BPs} m_k \mathbf{f}_k \quad (16)$$

The rotation matrix \mathbf{R} evolves according to

$$\frac{d}{dt} \mathbf{R} = \mathbf{R}\boldsymbol{\Omega} \quad (17)$$

where $\boldsymbol{\Omega}$ is a matrix filled with components of the angular velocity $\boldsymbol{\omega}$ which is defined in the object frame [19].

The change of angular velocity $\boldsymbol{\omega}$ in time is given by

$$\frac{d\boldsymbol{\omega}}{dt} = \mathbf{I}^{-1} \mathbf{R}^{-1} (\mathbf{T} - \mathbf{R}\boldsymbol{\Omega}\mathbf{I}\boldsymbol{\omega}) \quad (18)$$

where \mathbf{I} is the moments-of-inertia tensor in the object frame whose entries can be calculated from the geometry in the object frame, \mathbf{T} is the total external torque calculated in the world frame. In the simulation, we first compute the total force and torque on the floating object, \mathbf{F} and \mathbf{T} , and then update the floating object position according to Eq. (13) – Eq. (18). The position of any rigid body particle is then computed from Eq. (12).

The standard weakly compressible SPH method is known to loose accuracy in the vicinity of the boundaries and close to free-surfaces, where the normalization condition is not fulfilled. More advanced SPH schemes have been developed in order to overcome this problem, where these efforts are primarily concentrated on approaches which either correct the kernel and/or its first derivative [20,21], or by performing density filters, which can help to stabilize the pressure field [20,22–24]. Antuono *et. al* show that by adding a diffusive term in the continuity equation approximation, which is referred as δ -SPH method, the smoothness of the pressure field can also be improved [25]. However, although these enhanced SPH techniques demonstrate improved results, they are more computational intensive and hence considerably slower than the standard SPH [12]. In addition, there is a penalty in conservation when such techniques are used [12,26]. The purpose of this paper is not to investigate these improved methods, but to provide a simple but sufficiently accurate SPH framework for the study of wave impact on off-shore structures. From the results presented in next section, we show that the standard SPH is sufficient to fulfill this purpose, giving reasonably good result compared to the experimental data. Therefore, in this paper we adopt the standard weakly compressible SPH method [3,17,12].

3 Test cases

In this section we show two test cases. The first one is devoted to SPH simulation of wave impact force on a fixed structure [6], while the second one to floating body dynamics under the action of induced waves [9]. The accurate prediction of both cases is critical for the more complex simulation of an off-shore platform later.

3.1 Three dimensional dam break flow against a tall structure

In this section we present the validation of the SPH method for a typical three-dimensional dam break problem. Our purpose is to simulate a dam break experiment which was carried out by Yeh & Petroff [6]. The experiment provides data for the force of an impacting fluid surge, which can be compared with the force predicted by the SPH simulation. The experiments utilized a rectangular tank, 0.61 m wide, 1.6 m long, and 0.75 m high. A centrally located vertical column with a square 0.12 m profile is located 0.9 m from one end of the tank. A sketch of the experimental geometry is depicted in Fig. 1, the fluid used in experiment is water at ambient conditions. Water is held at a height of 0.3 m behind a gate which is raised to begin the experiment. Since it was not possible to completely evacuate the water from the tank, a 1 cm layer of water was present on the tank floor prior to the experiment.

As the fluid surge impacts upon the vertical column, attached load gauges report the impact force experienced by the column. Using an SPH model of this experiment, we compare the horizontal component of impact force predicted by the SPH method to that measured in the experiment.

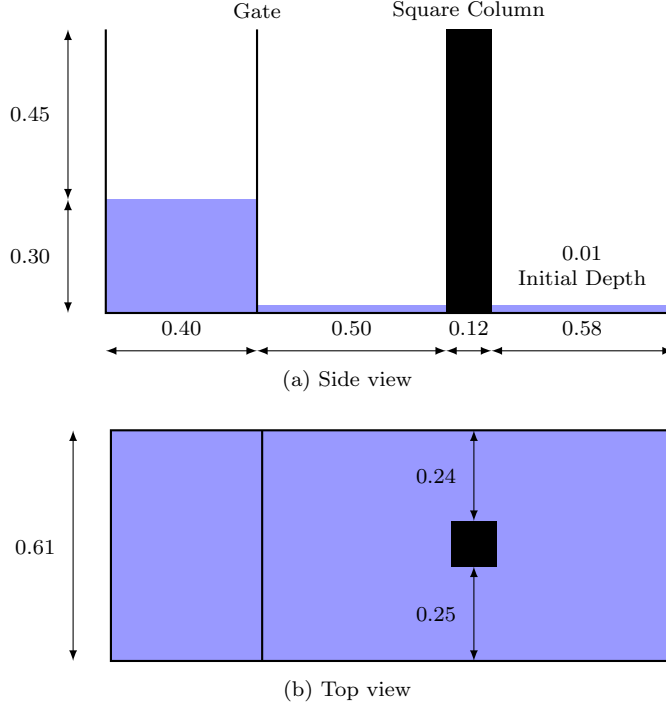


Fig. 1: Schematic diagram of the dam geometry (all dimensions in m) [6].

A sequence of snapshots of the particle positions is shown in Fig. 2, where particles are colored by velocity magnitude. The simulation shown was carried out with an initial particle spacing of 0.5 mm, which corresponds to a total number of approximately 800,000 fluid particles and 1,000,000 boundary particles. The sequence is as follows: First the fluid particles fall under the effect of gravity and flow with relatively high velocity towards the vertical column. Then, at approximately 0.3 seconds, they reach the vertical column. Some fluid particles impact upon the column before falling back, whereas the particles to the side of the tank will move past the column. After 1 second of simulation, a secondary impact upon the column occurs as the initial wave is reflected by the tank wall to the rear of the column.

The experimentally reported force data, which is shown in Fig. 3, reflect what can be observed visually in Fig. 2. In the first 0.3 seconds, the force is negligible because there is hardly any fluid touching the column. Then the first water surge arrives at the column, at 0.3 s, part of the fluid is decelerated and transfers its force onto the column. When the reflected wave passes the column, at approximately

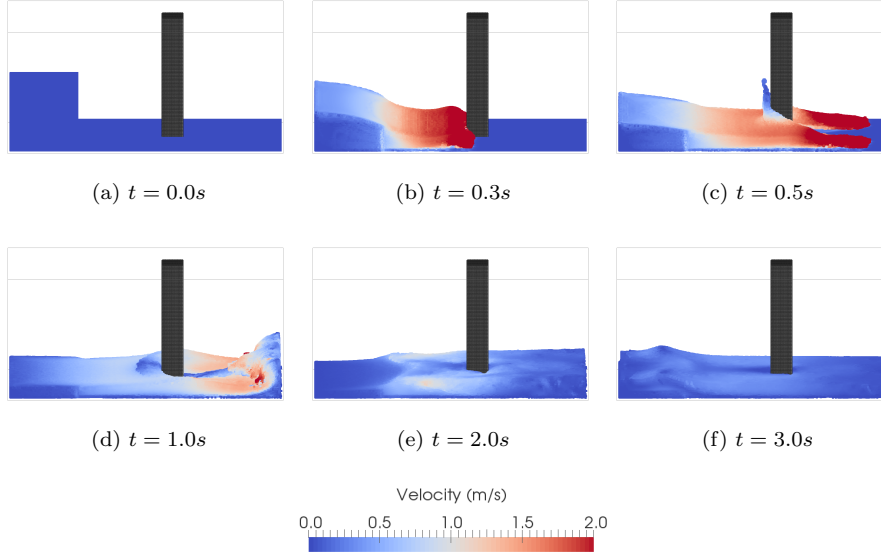


Fig. 2: Evolution of the water collapse and interaction with the column at various time steps.

1.3 seconds, a negative horizontal force is measured on the column. Finally the net horizontal force on the column settles around 0 N when the fluid is slowly coming to a standstill.

The horizontal force on the vertical column is plotted in Fig. 3 where a good agreement is obtained. Until 0.3 seconds, the force is practically 0 N, as expected. The height of the first peak is predicted rather well by the SPH simulation. This is in contrast with some other SPH simulation results reported in the literature [7], for example, had to use different filtering techniques to show agreement between their SPH results and the experimental data. Our SPH results, on the other hand, are generally quite close to the experimental data without any post-processing.

At 1.5 seconds, the secondary impact occurs roughly 0.25 seconds early in the SPH simulation. This was observed in other literature as well [6–8]. Authors in [6], who compared the experimental data with their own finite-volume simulation technique, point out that small bubbles are created in the experiment (presumably in regions of low pressure in the fluid), which in turn may slow down the speed of the reflected wave. Since these bubbles are not modeled in their numerical simulation method, the deceleration of the reflecting wave was not observed. Since our SPH simulation technique does not incorporate a model for bubble creation at low pressures, it does not pick up the same phenomenon, and the explanation in [6] is expected to be relevant for our simulation technique as well. In spite of this, our SPH result still shows better agreement with experimental data than some other results in the literature [8], for example, over-predicted the force on the obstacle after the initial wave impact.

Accurate prediction of the pressure field is important in impact force computation. A potential disadvantage of the WCSPH scheme is that it produces a noisy pressure field. This may be overcome by using the more advanced schemes mentioned previously however, due to the nature of the problem investigated herein, such techniques are not necessary. The reason for this is that we are primarily interested in the total force on a structure, and not the force at a particular point. In computing the total force on the structure a summation is carried out across all particles which make up the structure, smoothing the spatially varying noise observed when inspecting an individual particle or point. To smooth the high frequency time-variant noise, the average impact force over approximately 0.01 s of simulation time is taken. This approach maintains the computational efficiency of the WCSPH scheme, whilst comparing favorably with the experimental data as seen in Fig. 3.

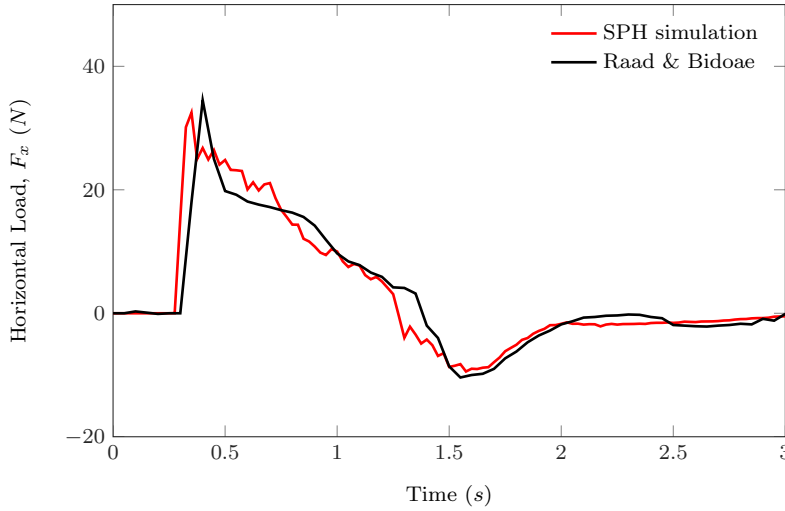


Fig. 3: Force calculation in 3D dam break case; comparison between SPH simulation result and experimental data [6].

3.2 Floating body dynamics under the action of induced wave

To fully capture the motion of offshore platforms we must ensure that we not only correctly capture the hydrodynamic loads on the structure, but that the motion of this structure is also correctly resolved and accounted for in the flow solution. As a validation case, we consider the experimental setup reported by Ruol *et. al* [9] and Manenti *et. al* [10]. In the work of Ruol *et. al* they carried out an experiment of a buoyant cube (representative of a waterbreak) secured by pile-mooring. Under the action of a periodic wave motion, both the vertical position of the cube, and upstream fluid surface height were recorded.

This experiment was designed to be Quasi-2D because the width of the waterbreak is approximately equivalent to the width of the tank. Manenti *et. al* also simulated this experiment in a 2D SPH model showing reasonable agreement. However, we note that in the experiment the waterbreak is allowed to roll to some extent, where this degree of freedom was not considered by Manenti *et. al*. We choose to include this extra degree of freedom in this work by applying the rigid-body-motion equations with the rotation matrix approach described in Eq. (12) – Eq. (18).

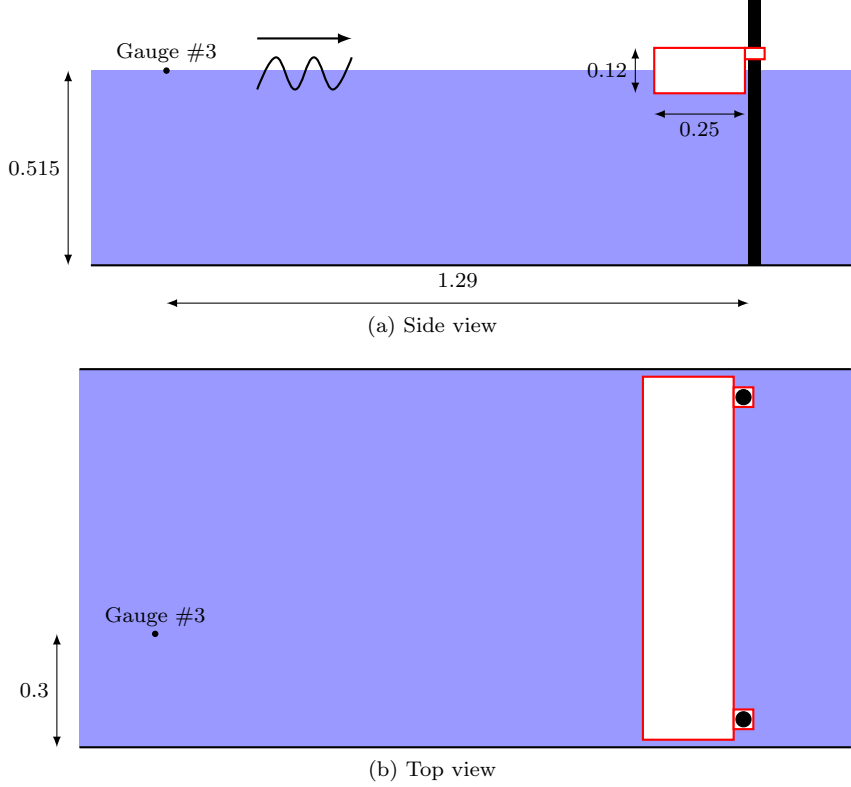


Fig. 4: Sketch of the plan view of the central part of the wave flume with the floating breakwater set up.

To illustrate the situation, the experimental configuration is shown in Fig. 4 and Fig. 5. The piston wave maker is located to the left of the domain, where it generates regular surface waves. The floating object is initially located 2 m downstream of the wave maker. The fluid used in the experiment is water with a density of 1000 kg/m^3 . The material and internal geometry of the floating object were chosen such that the effective density was 500 kg/m^3 , so that it is only half submerged while the system is at rest. Be advised that in the experiment the floating object was moored with piles such that it could not move horizontally.

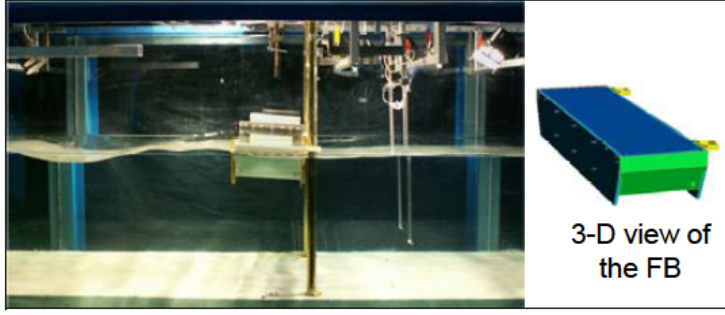


Fig. 5: Wave flume test with a pile-moored floating breakwater. Image reproduced from Manenti *et. al* [10].

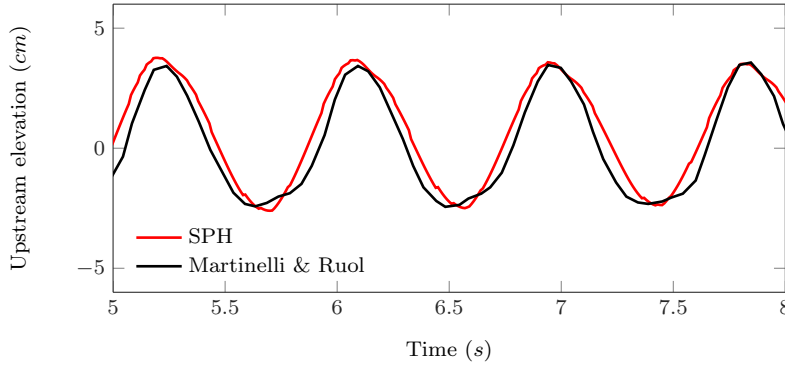
This experimental condition was reproduced in the SPH simulation by fixing the horizontal position of the center of mass of the floating object while keeping all other degrees of freedom (DOF) unrestricted, such as vertical displacement and rotation. The flat piston wave maker describes a sinusoidal motion in the horizontal direction with a frequency of 1.14 Hz and stroke of 0.05 m. Fig. 6 shows a side-view frame of the simulation at $t = 5$ s.



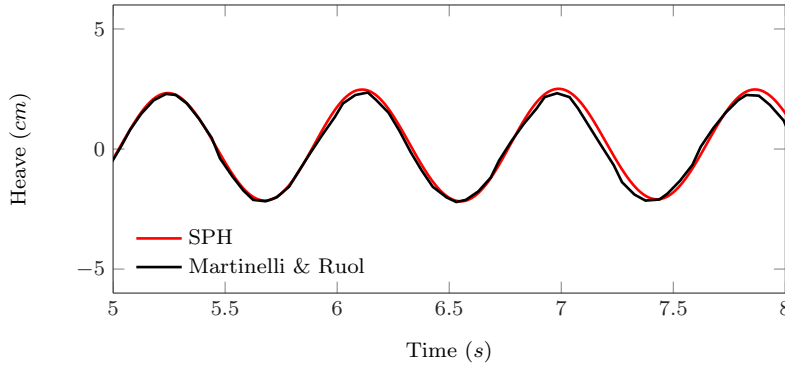
Fig. 6: Side view of SPH simulation of the wave flume test with a pile-moored floating breakwater at $t = 5$ s.

For quantitative comparison between the SPH model and laboratory results, the water surface elevation at gauge number 3 (Fig. 4) and heave displacements of the floating object have been considered at this stage of the analysis. Fig. 7a shows SPH calculated oscillations of the free surface at wave gauge number 3. The comparison with the experimental measures at steady condition shows good agreement of the signals frequency once the model achieves a steady state of periodic oscillation. Fig. 7b compares numerically calculated and measured heave oscillations of the floating breakwater. Phase angle and frequency are predicted with good accuracy as the model approaches a steady oscillation.

We believe the better agreement observed in our work compared to Manenti's result [10] is due to that, firstly, we included the modeling of the pile-mooring which prevents the floating from moving horizontally, and secondly, the buoyant cube was allowed to roll slightly about the horizontal axis as in the original experiment. If the rotational degree of freedom is neglected it is not possible to fully capture the



(a) Upstream elevation at gauge #3



(b) Heave of the floating breakwater

Fig. 7: Comparison between experimental data and numerical results for the floating breakwater.

behavior of the waterbreak driven by the induced wave, resulting in a discrepancy between the model and experimental results.

4 Application: Wave impact on a off-shore oil platform

As a proof-of-concept, we present a realistic application of the floating object model in this section. The objective is to study the effect of a solitary extreme wave impacting upon a tension-leg platform (TLP).

The geometrical configuration of the present simulation is shown in Fig. 8. The fluid basin is 50 m deep and stretches over a longitudinal distance of 800 m, and a transverse width of 150 m. The platform's center-of-mass is situated at a distance of 426 m from the initial position of the *moving boundary* particles used to generate the solitary wave, *i.e.* practically in the middle of the domain. The beach downstream of the platform, which is intended to prevent reflection of waves, starts at 600 m from the initial position of the moving boundary particles

and has an angle of 14° with the horizontal. In the transverse direction, the fluid is contained by rigid side walls.

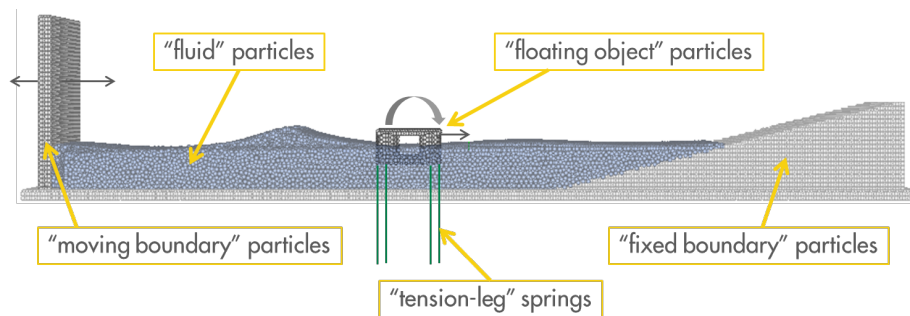


Fig. 8: Geometrical setup of three-dimensional simulation of an extreme wave hitting a platform.

A close-up of the SPH model of a floating platform is shown in Fig. 9. It consists of four vertical cylinders that, in reality, are mostly filled with air and keep the platform afloat. The cylinders are connected by pontoons. The top deck is modeled by a thin layer of particles. In principle one could add equipment at the top of the platform, but it has been left out here for the sake of simplicity. Nevertheless, all the critical parameters for the motion of the floating platform, namely the center-of-mass, the mass and the moments-of-inertia, are taken from a real platform. Therefore, the actual motion of the platform is still expected to be predicted fairly accurately, despite the lack of geometrical detail.

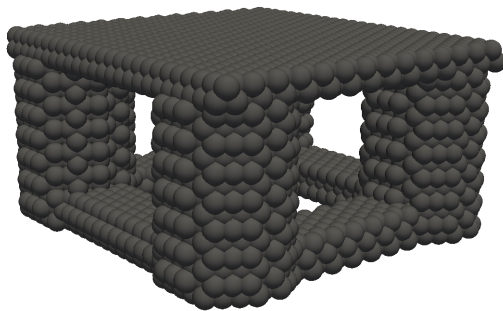


Fig. 9: Close-up of the platform model.

The platform is connected to the seabed by eight tension legs with two on each vertical cylinder of the platform. In the SPH simulation, tension legs are modeled as springs. Each of the springs is connected to an anchor point at the seabed at 500 m depth; although the sea bed is well outside the flow domain, this does not affect the validity of the spring equations. The points where the tension legs are attached to the platform are allowed to move in all three directions.

Each tension leg acts like a spring, with a spring constant, k_0 , and a nominal length of zero tension, L_0 . Each tension leg i provides the following force

$$\mathbf{F}_{TensionLeg,i} = -k_{0,i} (|\mathbf{x}_{attach,i} - \mathbf{x}_{anchor,i}| - L_{0,i}) \frac{\mathbf{r}_i}{|\mathbf{r}_i|} \quad (19)$$

where $\mathbf{x}_{attach,i}$ denotes the position of the attachment point of the tension leg at the platform and $\mathbf{x}_{anchor,i}$ denotes the location of the anchor at the sea bed. The force is precisely directed along the vector separating the attachment point and the anchor point with

$$\mathbf{r}_i = \mathbf{x}_{attach,i} - \mathbf{x}_{anchor,i} \quad (20)$$

The anchor points at the sea bed are aligned with the attachment points at the platform, so that the tension legs are perfectly vertical in the equilibrium situation. With the geometry chosen for the platform, the tension legs are slightly stretched in the equilibrium situation.

Because of the large spring constant, k_0 , a TLP is designed to have small vertical displacement under the wave impact as vertical displacement can be hazardous. Given this, it is expected that the horizontal displacement is larger than its vertical displacement. Therefore, it's useful to investigate the effect of tension legs when the platform is displaced horizontally. We first analyzed this problem by assuming that the platform has moved by a distance Δx , so that \mathbf{r}_i is equal to

$$\mathbf{r}_i = z_0 \mathbf{e}_z + \Delta x \mathbf{e}_x \quad (21)$$

Inserting Eq. (21) into Eq. (19) gives

$$\mathbf{F}_{T,i} = -k_{0,i} (|\mathbf{r}_i| - L_{0,i}) \frac{\mathbf{r}_i}{|\mathbf{r}_i|} = -k_{0,i} (|z_0 \mathbf{e}_z + \Delta x \mathbf{e}_x| - L_{0,i}) \frac{z_0 \mathbf{e}_z + \Delta x \mathbf{e}_x}{|z_0 \mathbf{e}_z + \Delta x \mathbf{e}_x|} \quad (22)$$

Fig. 10 shows the force components due to the eight tension legs in the platform geometry used in the SPH simulation.

To highlight this effect in some more detail, we expand Eq. (22) into a Taylor series up to third order. We investigate what happens if there is a horizontal displacement Δx . We can calculate the length of \mathbf{r}_i as

$$|\mathbf{r}_i| = \sqrt{z_0^2 + \Delta x^2} = z_0 \left(1 + \frac{1}{2} \epsilon^2 + \dots \right) \quad (23)$$

where ϵ is introduced as: $\epsilon = \Delta x / z_0$. With this, the horizontal forces become

$$\mathbf{F}_{T,i} \cdot \mathbf{e}_x = -k_{0,i} \left(z_0 + \frac{1}{2} z_0 \epsilon^2 - L_{0,i} \right) \left(\frac{\epsilon}{1 + \frac{1}{2} \epsilon^2} \right) \quad (24)$$

and the vertical force is:

$$\mathbf{F}_{T,i} \cdot \mathbf{e}_z = -k_{0,i} \left(z_0 + \frac{1}{2} z_0 \epsilon^2 - L_{0,i} \right) \left(\frac{1}{1 + \frac{1}{2} \epsilon^2} \right) \quad (25)$$

The estimates above are plotted in Fig. 10 which shows good agreement with the exact solution obtained from Eq. (22) given small horizontal displacement. Thus, in our simulation, the horizontal force is approximately linear in ϵ , with an important third-order term, whereas the magnitude of the vertical force is non-zero even if $\epsilon = 0$, and increases with a quadratic term in ϵ . Hence, any horizontal displacement is expected to cause a higher resulting force from the tension legs in the vertical direction than in the horizontal direction.

In summary, if the platform moves in the horizontal direction, the tension legs are stretched. In the horizontal direction, they tend to pull the platform back into position, but they also pull the platform down with even larger vertical force downward than its horizontal force component. This is a potential risk to a tension leg platform as it may end up being submerged by a forceful high sea wave. In our SPH simulations, we will investigate whether this effect is compensated by the buoyant force exerted by the fluid.

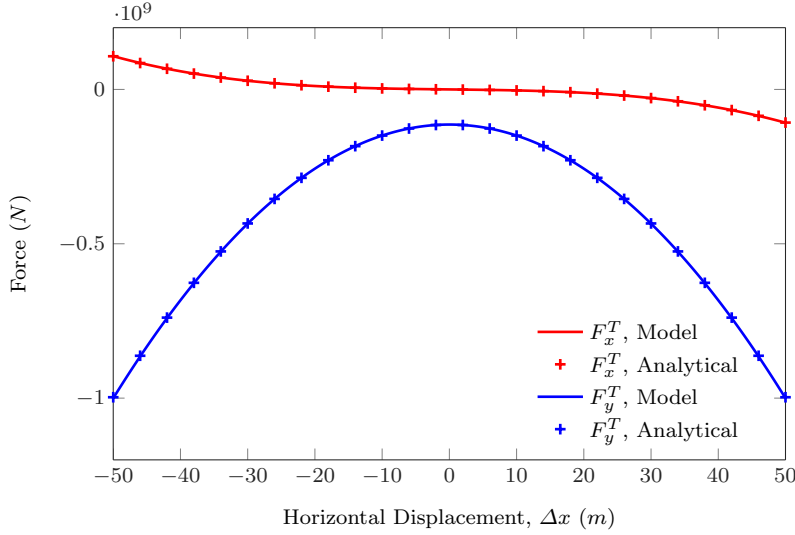


Fig. 10: Total force from eight tension legs, as a function of the horizontal displacement of the platform, for the realistic platform geometry.

We prescribe the displacement of the wave maker as a piston-like motion which follows a hyperbolic tangent function as:

$$\frac{\mathbf{x}_{piston}(t) - \mathbf{x}_{piston}(0)}{S} = \frac{1}{2} \left\{ 1 + \tanh \left(7.6 \left[\frac{t}{\tau} - \frac{1}{2} \right] \right) \right\} \quad (26)$$

where $S = 80$ m is piston stroke. Goring [27] derives that, for a perfect solitary wave, the time scale $\tau(S)$ should be:

$$\tau = \frac{(3.8 + \frac{3}{16}(S/d)^2)}{\sqrt{(1 + \frac{3}{16}(S/d)^2)(\frac{9}{64}(S/d)^2)}} \sqrt{d/g} \quad (27)$$

where $d = 50$ m is the water depth and g is gravitational acceleration. The resulting free-surface wave in the fluid is then a solitary wave of elevation according to reference [27–29].

Snapshots of the particle positions during the SPH simulation are shown in Fig. 11, at six instants of time. To better illustrate the flow about the platform, these results are presented in a zoomed view in Fig. 12. The fluid is colored by the local velocity magnitude. At the start of the simulation, $t = 0$ s, the fluid is at rest, but a solitary wave is formed within the first 20 seconds by moving the left boundary. The solitary wave travels with a velocity of approximately 25 m/s and reaches the platform around $t = 30$ s. Between $30 \text{ s} < t < 40 \text{ s}$, some water is flowing on the platform deck, while the platform is displaced towards the right. At $t = 40$ s, the solitary wave reaches the beach and dissipates, the fluid eventually comes to rest again, with the platform slowly moving back to its equilibrium position.

The displacement of the platform in the course of time is captured in Fig. 13. On the left-hand-side, we plot the three-dimensional motion as a function of time. It is clear that the highest displacement takes place in the x-direction (Surge) between 30 and 40 seconds of simulation time. This coincides with the moment the platform is hit by the solitary wave. After the wave has passed, the platform moves back towards its initial position but it overshoots a bit, so that it is located some 50 m left of its original position after 75 s. The overshooting is a characteristic of an under-damped mass-spring-damper system: the platform represents the mass here, the tension legs the springs and the fluid the damping mechanism of the motion.

The vertical displacement (Heave) increases between 20 and 25 seconds, as the platform is lifted up by the arriving wave. Quickly afterwards, however, the vertical displacement becomes negative, indicating that the platform is pulled into the water. This correlates with the horizontal displacement which causes the tension legs to pull the platform into the water, as explained in Eq. (25).

The trajectory of the platform, plotted in the right graph of Fig. 13, confirms the relation between horizontal and vertical displacement. The trajectory is similar to a parabola, with the vertical displacement approximately proportional to the horizontal displacement squared. This is in agreement with the analysis described above which is indicated by Fig. 10.

Since the total force on the platform is equal to the sum of the force by the tension legs plus the force by the fluid plus gravity, it is now also possible to extract information on the force exerted by the fluid on the platform; it is shown in the left graph of Fig. 14. The right graph of Fig. 14 shows the force from the tension legs. The result suggests that the fluid exerts a much larger force on the platform in the upward direction (buoyant force) than in the horizontal direction, even when the wave hits the platform. The main contribution of the fluid is thus to keep the platform afloat. Comparison between the left graph and right graph of Fig. 14 shows that the fluid provides upward lift when the tension legs pull the platform into the water.

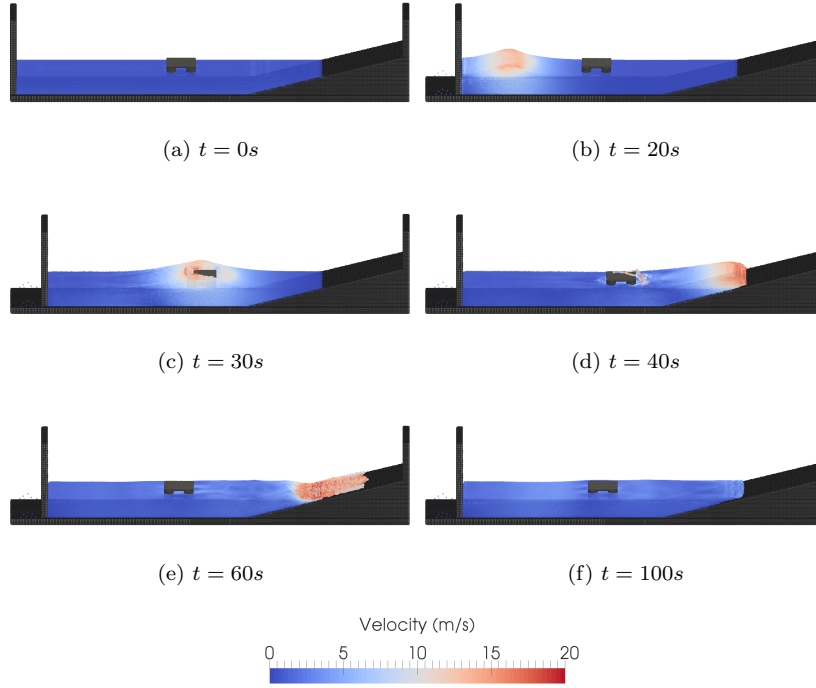


Fig. 11: Six snapshots of the SPH simulation with a moving platform (3D view). The fluid is colored by velocity magnitude. The solid side walls are not shown for better visualization.

Finally, the rotation of the platform during the simulation is shown in Fig. 15. The pitch (rotation around the y-axis) is highest precisely when the wave arrives around $t = 25$ s, as could be expected. The actual pitch rotation, however, is extremely small, it has a maximum of 0.6° . The reason for this extremely low value is because a stretched tension leg exerts a larger force than a tension leg in its equilibrium position, any rotation in the x-direction (roll) or y-direction (pitch) is directly counteracted. Therefore, it is no coincidence that the largest rotation angles are observed in the z-direction (yaw), it is the only direction where the rotation is not efficiently counteracted by the spring-like tension legs.

This model shows that the result of rogue wave impact may be counterintuitive. Though the platform rose upon initial impact, it quickly became submerged. It also shows that a tension-leg platform is very unlikely to topple over during the arrival of an extreme wave, at least for the design parameters used during the present simulation. A model like this can serve as a stepping stone for more advanced simulations in the future, where the platform can be modeled in more detail and the sea can be modeled in better agreement with real oceanographic data.

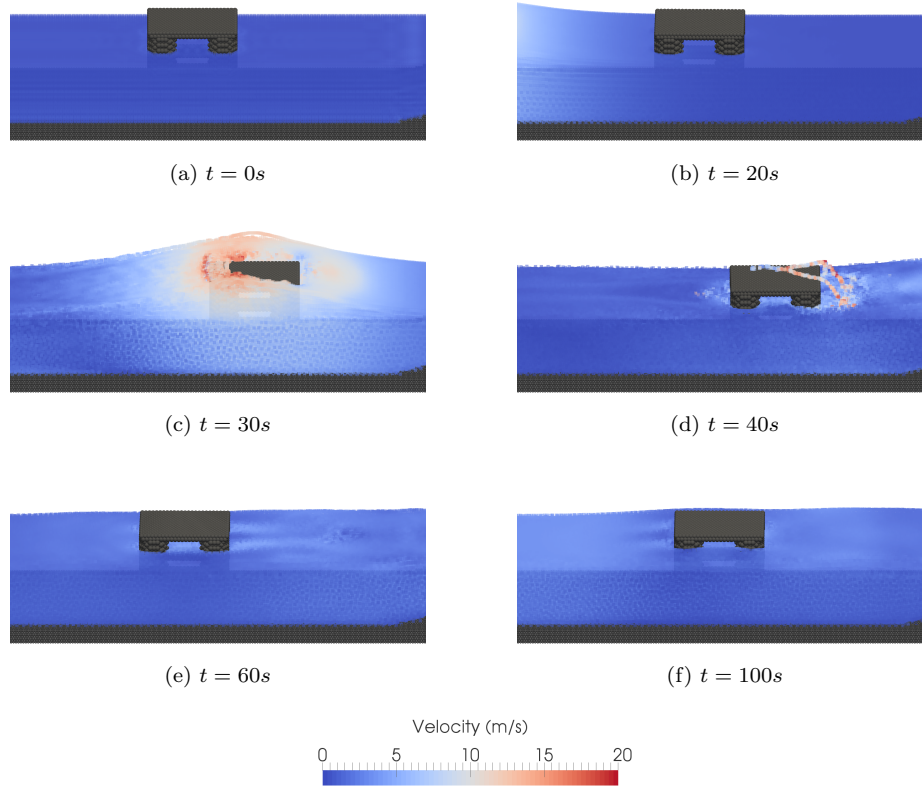


Fig. 12: Six snapshots of the SPH simulation with a moving platform (zoomed view of platform).

5 Conclusion

Two validation cases and a realistic design experiment have been performed using the SPH method. Validation of dam-break flow with a rectangular column located downstream shows that results were in good agreement with the experimental data. Oscillations in the column forces after both the first and the secondary impact were well captured. The simulations demonstrate the ability of SPH to reproduce the complex transient loading characteristic of inertial and gravity driven flow on fixed structures.

We have also validated the SPH simulation against an experiment which measures the vertical displacement of a rectangular object forced by regular waves. We show that the heave of the floating object and the wave elevation was in excellent agreement with experimental data.

Finally, we applied the SPH simulation to a real-world application to study the effect of a single solitary wave hitting a tension-leg platform. The impact force

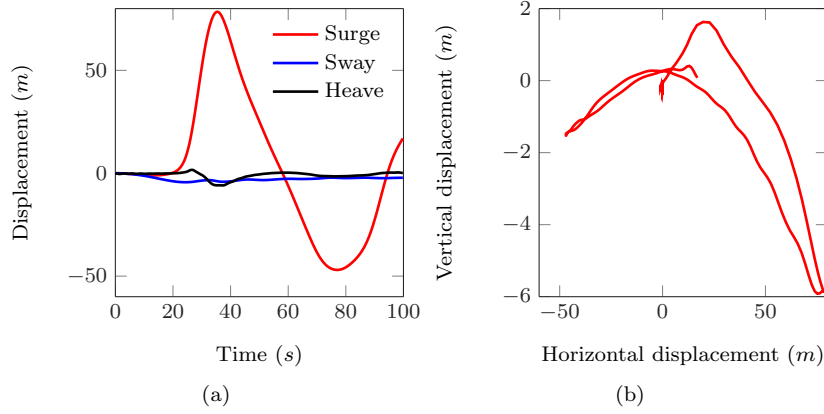


Fig. 13: Results from the SPH simulation with a moving platform. (a) Displacement of the platform's center-of-mass in x-direction (Surge), y-direction (Sway) and z-direction (Heave). (b) Position of the platform's center-of-mass in the xz-plane during the simulation.

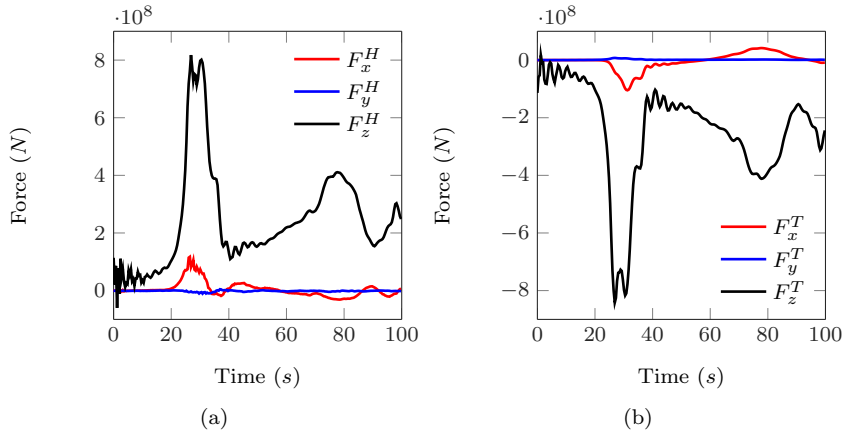


Fig. 14: Results from the SPH simulation with a moving platform. Left: forces exerted by the fluid on the platform in x-direction, y-direction and z-direction. Right: forces exerted by the tension legs on the platform in x-direction, y-direction and z-direction.

due to the wave and the reaction force exerted by the tension legs were analyzed separately in detail. Also studied was the horizontal and vertical displacement of the platform under the effect of a sea wave and tension legs. This analysis shows that the platform may be pulled into the water by stretched tension legs, where the extension of the tension legs also governs the rotational behavior of the platform.

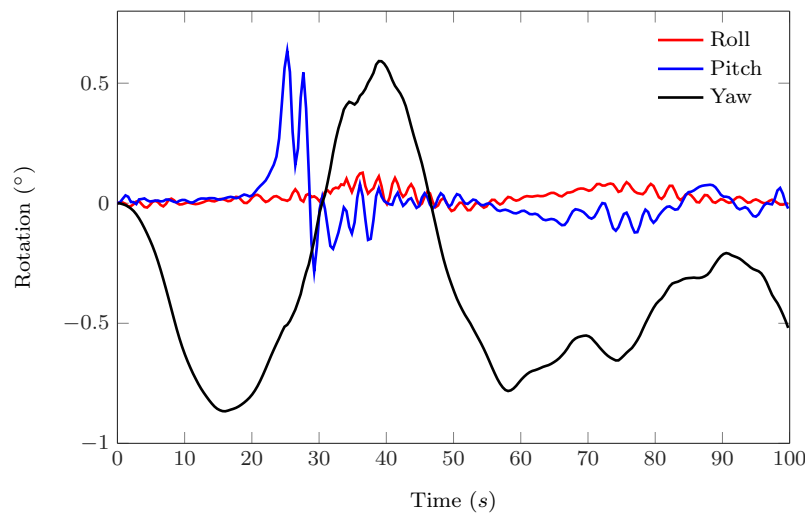


Fig. 15: Results from the SPH simulation with a moving platform: platform rotation as a function of time.

This simulation can serve as a blueprint for more advanced simulations in the future where the platform model may include more detail, and the initial state of the fluid phase may be more representative of conditions observed in oceans.

References

1. S Lehner and W Rosenthal. Investigation of ship and platform accidents due to severe weather events: Results of the maxwave project. In *25th International Conference on Off-shore Mechanics and Arctic Engineering*, pages 753–760. American Society of Mechanical Engineers, 2006.
2. Joe J Monaghan. Simulating free surface flows with sph. *Journal of computational physics*, 110(2):399–406, 1994.
3. JJ Monaghan. Smoothed particle hydrodynamics and its diverse applications. *Annual Review of Fluid Mechanics*, 44:323–346, 2012.
4. Gui-Rong Liu and Moubin B Liu. *Smoothed particle hydrodynamics: a meshfree particle method*. World Scientific, 2003.
5. MB Liu and GR Liu. Smoothed particle hydrodynamics (sph): an overview and recent developments. *Archives of computational methods in engineering*, 17(1):25–76, 2010.
6. Peter E Raad and Razvan Bidoae. The three-dimensional eulerian–lagrangian marker and micro cell method for the simulation of free surface flows. *Journal of Computational Physics*, 203(2):668–699, 2005.
7. SJ Cummins, TB Silvester, and Paul W Cleary. Three-dimensional wave impact on a rigid structure using smoothed particle hydrodynamics. *International journal for numerical methods in fluids*, 68(12):1471–1496, 2012.
8. M Gómez-Gesteira and Robert A Dalrymple. Using a three-dimensional smoothed particle hydrodynamics method for wave impact on a tall structure. *Journal of waterway, port, coastal, and ocean engineering*, 130(2):63–69, 2004.
9. Piero Ruol and Luca Martinelli. Wave flume investigation on different mooring systems for floating breakwaters. *Submitted to Coastal Structures*, 7, 2007.
10. S Manenti and P Ruol. Fluid-structure interaction in design of offshore wind turbines: Sph modeling of basic aspects. In *Proc. Int. Workshop Handling Exception in Structural Engineering*, pages 13–14, 2008.

11. Joseph P Morris, Patrick J Fox, and Yi Zhu. Modeling low reynolds number incompressible flows using sph. *Journal of computational physics*, 136(1):214–226, 1997.
12. Joe J Monaghan. Smoothed particle hydrodynamics. *Reports on progress in physics*, 68(8):1703, 2005.
13. Moncho Gomez-Gesteira, Benedict D Rogers, Alejandro JC Crespo, RA Dalrymple, M Narayanaswamy, and José M Dominguez. Sphysics–development of a free-surface fluid solver–part 1: Theory and formulations. *Computers & Geosciences*, 48:289–299, 2012.
14. Alejandro C Crespo, Jose M Dominguez, Anxo Barreiro, Moncho Gómez-Gesteira, and Benedict D Rogers. Gpus, a new tool of acceleration in cfd: Efficiency and reliability on smoothed particle hydrodynamics methods. *PLoS One*, 6(6):e20685, 2011.
15. Joe J Monaghan. Smoothed particle hydrodynamics. *Annual review of astronomy and astrophysics*, 30:543–574, 1992.
16. George Keith Batchelor. *An introduction to fluid dynamics*. Cambridge university press, 2000.
17. Moncho Gomez-Gesteira, Benedict D Rogers, Robert A Dalrymple, and Alex JC Crespo. State-of-the-art of classical sph for free-surface flows. *Journal of Hydraulic Research*, 48(S1):6–27, 2010.
18. AJC Crespo, M Gómez-Gesteira, and Robert A Dalrymple. Boundary conditions generated by dynamic particles in sph methods. *CMC-TECH SCIENCE PRESS-*, 5(3):173, 2007.
19. James L Meriam and L Glenn Kraige. *Engineering mechanics: dynamics*, volume 2. John Wiley & Sons, 2012.
20. T Belytschko, Y Krongauz, J Dolbow, and C Gerlach. On the completeness of meshfree particle methods. *International Journal for Numerical Methods in Engineering*, 43(5):785–819, 1998.
21. Gary A Dils. Moving-least-squares-particle hydrodynamicsi. consistency and stability. *International Journal for Numerical Methods in Engineering*, 44(8):1115–1155, 1999.
22. J Bonet and T-SL Lok. Variational and momentum preservation aspects of smooth particle hydrodynamic formulations. *Computer Methods in applied mechanics and engineering*, 180(1):97–115, 1999.
23. JP Vila. On particle weighted methods and smooth particle hydrodynamics. *Mathematical models and methods in applied sciences*, 9(02):161–209, 1999.
24. JK Chen and JE Beraun. A generalized smoothed particle hydrodynamics method for nonlinear dynamic problems. *Computer Methods in Applied Mechanics and Engineering*, 190(1):225–239, 2000.
25. M Antuono, Andrea Colagrossi, and S Marrone. Numerical diffusive terms in weakly-compressible sph schemes. *Computer Physics Communications*, 183(12):2570–2580, 2012.
26. GL Vaughan, Terry R Healy, Karin R Bryan, Alfred D Sneyd, and RM Gorman. Completeness, conservation and error in sph for fluids. *International journal for numerical methods in fluids*, 56(1):37–62, 2008.
27. Derek Garard Goring. *Tsunamis–the propagation of long waves onto a shelf*. PhD thesis, California Institute of Technology, 1978.
28. Costas Emmanuel Synolakis. Generation of long waves in laboratory. *Journal of waterway, port, coastal, and ocean engineering*, 116(2):252–266, 1990.
29. Morteza Anbarsooz, Mohammad Passandideh-Fard, and Mohammad Moghiman. Fully nonlinear viscous wave generation in numerical wave tanks. *Ocean Engineering*, 59:73–85, 2013.